Journal of Materials Chemistry A

ROYAL SOCIETY OF CHEMISTRY

PAPER

View Article Online
View Journal | View Issue

Cite this: J. Mater. Chem. A, 2023, 11, 16263

Understanding the role of non-fullerene acceptor crystallinity in the charge transport properties and performance of organic solar cells†

Pierluigi Mondelli, ‡*[ad] Pascal Kaienburg, [a] Francesco Silvestri,[b] Rebecca Scatena, [a] Claire Welton,[c] Martine Grandjean, [d] Vincent Lemaur, [e] Eduardo Solano, [f] Mathias Nyman,[g] Peter N. Horton,[h] Simon J. Coles, [h] Esther Barrena, [b] Moritz Riede,[a] Paolo Radaelli,[a] David Beljonne, [e] G. N. Manjunatha Reddy [c] and Graham Morse *[d]

The acceptor crystallinity has long been associated with favourable Organic Solar Cell (OSC) properties such as high mobility and fill factor. In particular, this applies to acceptor materials such as fullerene derivatives and the most recent Non-Fullerene Acceptors (NFAs), which are now surpassing a Power Conversion Efficiency (PCE) of 19%. Although these advantages are commonly attributed to their 3-dimensional crystal packing motif in the single crystal, the bridge that links the acceptor crystal packing from single crystals to solar cells has not clearly been shown yet. In this work, we investigate the molecular organisation of seven NFAs (*o*-IDTBR, IDIC, ITIC, *m*-ITIC, 4TIC, 4TICO, and *m*-4TICO), following the evolution of their packing motif in single-crystals, powder, and thin films made with pure NFAs and donor:NFA blends. We observed a good correlation between the NFA single crystal packing motif and their molecular arrangement in the bulk heterojunction. The NFA packing motif affects the material's propensity to form a highly crystalline domain in the blend. We specifically found that 3D reticular packing motifs show stronger ordering than 0D herringbone ones. However, the NFA packing motif is not directly correlating with device performance parameters. Although higher NFA crystallinity yields higher mobility, we found the domain purity to be more important for obtaining high efficiency organic solar cells by governing bimolecular recombination.

Received 2nd June 2023
Accepted 4th July 2023

DOI: 10.1039/d3ta03284a

rsc.li/materials-a

Introduction

The recent surge in OSC performance, now exceeding 19%,[1,2] results from the development of NFAs.[3–8] Previous work centred around fullerene based acceptors has drawn a connection between the molecular design/shape and the formation of highly interconnected acceptor domains and charge percolation pathways towards the electrodes, resulting in superior charge transport properties and high Fill Factors (FF) in OSCs.[9–12] Moreover, recent studies attributed the improved performance and charge transport of state of the art NFAs to their 3D-interconnected crystal packing motif (Fig. 1).[5,7–9,13–18] It is thus important to develop a clear understanding based on concrete evidence of the relationship between the NFA molecular packing and crystallinity in the bulk heterojunction and the charge transport properties and performance of OSCs.

A growing variety of NFA single-crystals are now being reported,[8,14,15,19–32] from which useful information on the molecular packing can be derived. Still, bridging the molecular scale from molecular packing in single-crystals to the one found in Bulk Heterojunctions (BHJs) needs more detailed investigations.[10,32,33] The identification of the packing motif of the NFA within

[a]Clarendon Laboratory, Department of Physics, University of Oxford, Parks Road, Oxford, OX1 3PU, UK. E-mail: pierluigi.mondelli@physics.ox.ac.uk

[b]Institut de Ciència de Materials de Barcelona, ICMAB-CSIC, Campus UAB, 08193 Bellaterra, Spain

[c]University of Lille, CNRS, Centrale Lille, Univ. Artois, UMR 8181 – UCCS – Unité de Catalyse et Chimie du Solide, F-59000 Lille, France

[d]Merck Chemicals Ltd, Chilworth Technical Centre, University Parkway, Southampton, SO16 7QD, UK. E-mail: pierluigi.mondelli@gmail.com; graham.morse@gmail.com

[e]Laboratory for Chemistry of Novel Materials, University of Mons, Place du Parc, 20, 7000 Mons, Belgium

[f]ALBA Synchrotron Light Source, NCD-SWEET beamline, Cerdanyola del Vallès, 08290, Spain

[g]Physics, Faculty of Science and Engineering, Åbo Akademi University, 20500 Turku, Finland

[h]EPSRC Crystallographic Service, Department of Chemistry, University of Southampton, Highfield, SO17 1BJ, UK

† Electronic supplementary information (ESI) available. CCDC 2236094 and 2226731. For ESI and crystallographic data in CIF or other electronic format see DOI: https://doi.org/10.1039/d3ta03284a

‡ Current address: Italian Institute of Technology, Printed and Molecular Electronics, Via Pascoli 70/3, 20133 Milan, Italy.

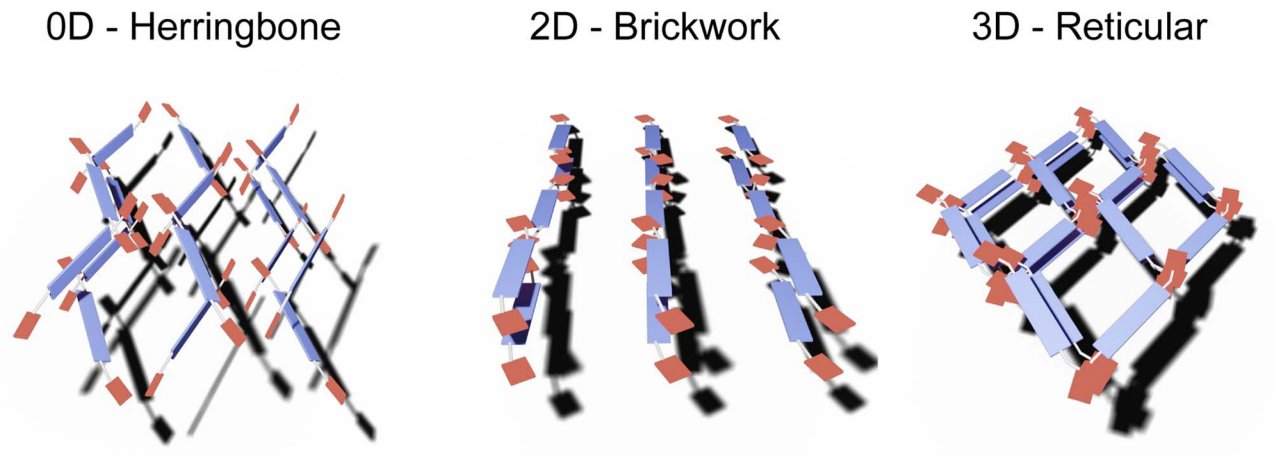

Fig. 1 Sketch of the different molecular packing motifs observed in Acceptor–Donor–Acceptor (A–D–A) type NFA crystal structures and labelled according to the dimensionality of the π–π stacking.

a donor:acceptor blend is a challenging task, yet the structural analysis is commonly based on Grazing Incidence Wide Angle X-ray Scattering (GIWAXS) patterns that lack enough diffraction features for the structural determination. The analysis of the main Bragg peaks of the NFA, often referred to as the lamellar (100) and the π–π stacking (010) distances,[34–36] is routinely considered enough to draw conclusions. Misleading results can, however, arise from the similar (if not overlapping) spectral features of the donor and acceptor components in the *q*-space, the typical peak broadening of organic compound isomers, polymorphism,[37,38] and a general lack of long-range crystalline order.[35]

In this work, we used an extensive set of both experimental and theoretical approaches to study the molecular packing and morphology of a specific set of common NFAs (*o*-IDTBR, IDIC, ITIC, *m*-ITIC, 4TIC, 4TICO, and *m*-4TICO, whose structures are shown in Fig. 2), by means of single-crystal X-ray diffraction (XRD), powder XRD and Le Bail refinement, GIWAXS, Atomic Force Microscopy (AFM), crystal lattice simulations, solid-state NMR spectroscopy (ss-NMR), and Gauge Including Projected Augmented Wave (GIPAW) DFT calculations. Our aim was to analyse the NFA molecular packing, with a special focus on the structural evolution from single crystals to solar cells. We studied the molecular arrangement from single crystals, to powders, and then thin films and finally the morphology in the bulk heterojunction (BHJ) to provide important insights into the NFA arrangement in the BHJs. We analysed the most relevant NFA packing motifs and polymorphs, discussing their role in the solar cell morphology, current–voltage performance, and

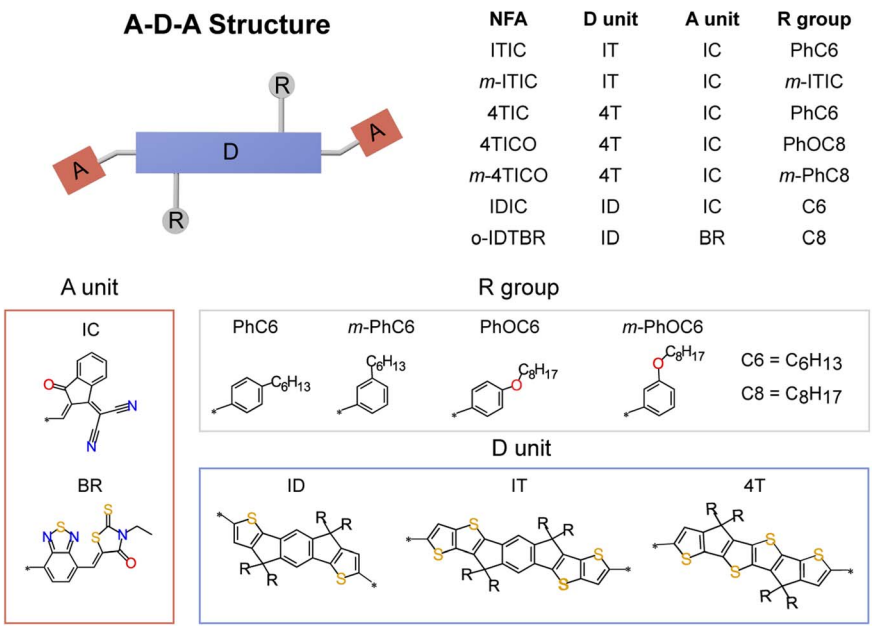

Fig. 2 Structure of an Acceptor–Donor–Acceptor (A–D–A) NFA with its building blocks on the top left. The NFAs studied in this work (table on the top right) are identified with their chemical subunits (A, D and R groups) whose chemical structures are also shown.

charge transport properties, such as electron mobility and bimolecular recombination, by means of photo-CELIV (Charge Extraction Linear Increasing Voltage) and MIS-CELIV (Metal–Insulator–Semiconductor-Charge Extraction Linear Increasing Voltage).

Experimental

General characterisation

UV-vis absorption spectra were recorded on an OceanOptics QE PRO spectrometer using a tungsten halogen light source (HL-2000-FHSA from OceanOptics). The HOMO levels of the compounds in thin films were obtained by measuring the film photoemission current onset with the Air Photoemission Spectroscopy module (APS02) of the Kelvin Probe from KP Technology Ltd. The Kelvin Probe was equipped with a 2.0 mm diameter tip coated with gold alloy, a UV deuterium lamp, and a monochromator (range 3.44–3.88 eV). LUMO levels were estimated by adding the optical bandgap (determined from the onset of the UV-vis absorption) to the measured HOMO.

IDIC single-crystal X-ray diffraction data were collected on a Rigaku Oxford Diffraction Supernova diffractometer equipped with a micro-focus sealed (Mo Kα) X-ray Source, CCD plate detector and Oxford Cryostream N2 flow cryostat. The *m*-4TICO crystal (CCDC deposition number 2236094) was collected on a Rigaku FRE+ diffractometer equipped with VHF Varimax confocal mirrors and an AFC12 goniometer and HyPix 6000 detector. The samples were mounted on Kapton loops from the solution and shock-cooled to 173.0(2) K or 100.0(2) K. Cell indexing and peak integration were performed with CrysAlisPro. Structural solution and refinement were carried out with ShelxT and ShelxL, respectively.

Powder X-ray diffraction was performed using a PANalytical X'Pert PRO diffractometer with Cu Kα radiation. During the measurement, the sample was kept at room temperature and under ambient conditions.

GIWAXS

The GIWAXS experiments were carried out at the NCD-SWEET beamline at the ALBA synchrotron (Beamtime ID: 2019093873). A monochromatic X-ray beam with a photon energy of 12.4 keV was set using a Si (1 1 1) channel cut monochromator, further collimated with an array of beryllium lenses. The GIWAXS maps were recorded with a Rayonix LX 255-HS detector, consisting of a pixel array of 960 × 2880 pixels of 88.54 × 88.54 μm^2 (H × V) for the binning employed. The samples were thermally annealed before the measurements at the optimised temperature for the solar cell performance (see below) using a hotplate in air. GIWAXS frames were acquired near the critical angle of the glass substrate (*ca.* 0.15° for the X-ray wavelength employed), penetrating a depth of 11 nm for the layer of interest,[39] while minimizing the contribution of the substrate.§ The recorded 2D scattering patterns were analysed using a home-made python routine based on pyFAI (the fast azimuthal integration Python library).[40] GIWAXS images are on a logarithmic scale, ranging from dark blue (low intensity) to yellow (high intensity). The in-plane and out-of-plane profiles were obtained by integrating the diffraction intensity in rectangular areas centred at $\chi = 0°$ and $\chi = 90°$ from χ–q images (scattering intensity as a function of the azimuthal angle). The scattering peaks of the bulk structure were compared to the experimental data using SimDiffraction, a MatLab code[41] for simulating the film diffraction pattern for a given crystal structure and orientation.[42] For each NFA, the simulations were performed by choosing a specific NFA orientation with respect to the substrate (typically in-plane and out-of-plane). The Miller indices (*h k l*) associated with the NFA packing direction were determined by Mercury[43] and used as input parameters for the simulations. A better fit between simulated and experimental GIWAXS was obtained when using the unit cell parameters obtained by Le Bail refinement (see below) as input for the simulations.

Solid-state NMR spectroscopy

For ssNMR experiments, O-IDTBR powder was packed into a 1.3 mm (outer diameter) rotor. All 1D ^{1}H and ^{13}C, and 2D ^{1}H–^{1}H and ^{1}H–^{13}C correlation NMR experiments were carried out on a Bruker Avance Neo (18.8 T) spectrometer using a 1.3 mm double resonance H-X probehead tuned to ^{1}H (Larmor frequency, 800.1 MHz, unless otherwise stated) and ^{13}C (Larmor frequency, 201.2 MHz) nuclei. Unless otherwise stated, the Magic Angle Spinning (MAS) frequency was 50 kHz in all cases. The nutation frequencies for ^{1}H and ^{13}C were 100 kHz and 90 kHz, corresponding to 90° pulse durations of 2.5 and 2.75 μs, respectively. The longitudinal relaxation time (T_1) of ^{1}H was determined to be 3 s based on inversion recovery measurements and analyses. The 1D ^{1}H MAS NMR spectrum was acquired using 16 co-added transients. A 2D ^{1}H–^{1}H double-quantum (DQ)-single-quantum (SQ) NMR spectrum was acquired using the Back-to-Back (BaBa) sequence at fast MAS,[44] using a rotor-synchronized t_1 increment of 20 μs corresponding to one rotor period (τ_r). The indirect ^{1}H DQ dimension was acquired using 256 t_1 increments, each with 16 co-added transients, corresponding to a total experimental time of ~4 h. ^{1}H detected 2D ^{1}H–^{13}C heteronuclear correlation (HETCOR) spectra were acquired with CP contact times of 0.1 ms and 3 ms and the indirect ^{13}C dimension was acquired using 140 t_1 increments, each with 32 co-added transients, corresponding to a total experimental time of 8 h each.

Atomic force microscopy

The thin films were investigated by AFM both in contact and dynamic modes using a commercial head and control unit from Nanotec Electronica. The used thermal annealing protocol was the one optimized for the devices (see Table S10†). For each sample, after each annealing step, different spots of the surface were imaged (at several image sizes) to have a statistical validity of the measurements. The images presented in the article are chosen as high-resolution representative images of the surface.

§ Cu Kα X-ray penetration depth on our films is ~11 nm for incident angles $\alpha = 0.11°$ (assuming the same critical angle of $\theta_c = 0.17°$).

Table 1 Crystallographic information of the NFA crystal structures available for the materials analysed in this work

CCDC Identifier	Molecule	Motif	π–π	a (Å)	b (Å)	c (Å)	α (deg)	β (deg)	γ (deg)	Volume (Å^3)
FOSPOV[58]	*o*-IDTBR	Reticular	3D	13.7663(2)	15.81032(17)	32.7146(3)	90	96.2928(12)	90	7077.43(15)
YEBKEY[20]	4TIC	Reticular	3D	13.969(7)	17.144(9)	17.970(10)	104.668(16)	109.998(17)	96.169(14)	3822.08
VUBJIO[19]	*m*-4TICO	Brickwork	2D	8.6526(3)	16.4878(8)	18.0435(8)	114.697(5)	103.822(4)	90.890(4)	2251.45(19)
2236094	*m*-4TICO	Brickwork	2D	8.7845(7)	15.3726(13)	16.7896(13)	67.136(7)	85.678(7)	79.630(7)	2055.0(3)
VUBJOU[19]	*m*-ITIC	Brickwork	2D	8.7454(13)	18.872(2)	25.2647(18)	87.770(8)	88.724(9)	78.001(12)	4075.1(9)
VUBKAH[19]	IDIC	Brickwork	2D	8.6679(4)	12.5073(7)	13.5784(6)	72.096(4)	75.545(4)	88.839(4)	1353.88(12)
VUBJEK[19]	4TICO	Herringbone	0D	15.2836(2)	20.0101(5)	29.3242(6)	90	89.997(2)	90	8968.1(3)
KIZSUK[21]	ITIC	Brickwork	2D	8.420(6)	23.019(17)	23.126(17)	101.780(10)	95.319(10)	91.105(14)	4366(5)
HEHQUJ01 (ref. [19])	ITIC	Herringbone	0D	14.9009(7)	15.5043(4)	18.1199(5)	99.309(2)	101.541(3)	108.366(3)	3777.2(2)

The estimation of the root mean square (RMS) roughness was done selecting about 6 contact mode images (30 × 30 and 50 × 50 μm^2) for each temperature. Si_3N_4 V-shaped cantilevers (Veeco) with the nominal force constant ranging between 0.03 and 0.5 N m^{-1} were employed for the contact mode, while Cr/Pt-coated silicon tips on rectangular cantilevers (BudgetSensors) with a nominal resonance frequency of 75 kHz and a force constant of 3 N m^{-1} were used for the dynamic mode. Open-source Gwyddion software was used to analyse all the presented AFM images,[45] including the domain size calculation which were done using the watershed algorithm.[46] The input parameters used for the watershed analysis can be found in the ESI† (pages S20–S25).

Solar cell fabrication and characterisation

Inverted-architecture organic solar cells were fabricated by blade coating of the organic layers on Indium Tin Oxide (ITO)/glass pre-patterned 5 × 5 cm^2 substrates (Zencatec Limited). A detailed description of the fabrication of the interlayers and electrodes, along with the experimental description of the current–voltage (*I–V*) measurements can be found in the experimental section of recent work from our group.[37] Aluminium-doped zinc oxide from Avantama (N-21X-Slot) was used for the electron transporting layer, while PEDOT:PSS (Clevios Al 4083 from Heraeus) for the hole transporting layer. All the NFAs were supplied by 1-Material Inc., with the only exception of 4TICO (Merck KGaA). For the active layer, PBTZT-stat-BDTT-8 (Merck KGaA) was used as the donor material[47] in combination with the NFAs listed in Fig. 2. Each blend was dissolved in a 1 : 1.3 ratio (by weight) and 80 nm thick layers¶ were processed from a 23 mg ml^{-1} solid content *o*-xylene solution, without the use of additional additives. The blade speed was adjusted between 7 and 13 mm s^{-1} to reach the desired thickness with a 100 μm blade gap and 70 μL cast volume. Casting plate temperature was varied between 60 °C and 80 °C and the as-cast devices were further annealed at temperatures ranging from 100 °C to 140 °C on a hot plate in air following the optimisation protocol. A 100 nm silver back electrode was thermally evaporated on top of the hole transporting layer, under a pressure of 2 × 10^{-6} mbar at a rate of 1 Å s^{-1}. Solar cells have a device area of ∼8.5 mm^2, as determined from the geometrical overlap between the cathode and anode.

¶ The active layer thickness was determined by using a Veeco DEKTAK 150 surface profilometer.

Photo-CELIV

Photo-CELIV was performed using the Transient Measurement Unit from Automatic Research. A 655 nm laser pulse (5 μs long) was used to photo-generate charges into ∼8.5 mm^2 area solar cells. The linear increasing voltage ramp range was 0–1.5 V and 10 μs long. The delay time between the laser pulse and the voltage ramp was varied between 0.1 and 100 μs, during which a constant pre-bias voltage (close to V_{OC}) was applied to limit the charge injection. The charge mobility was determined by using eqn (24) of ref. [48] on the 30 μs long delay time data collection. The bimolecular recombination coefficient was calculated using eqn (2) of ref. 49.

MIS-CELIV

MIS-CELIV[50] was performed with a PAIOS system from Fluxim AG, Switzerland. The layer stack was ITO/AZO/active layer/MgF_2/Ag with an insulating 50 nm MgF_2 layer that blocks the injection of holes so that the electron mobility is obtained. The chosen thickness balances the layer's insulating properties with its capacitance in relation to the absorber's capacitance. The other layers are processed as for the solar cell devices with some deviations in the annealing protocol discussed in the ESI.† A small device area of ∼1 mm^2 was chosen to minimize RC effects. The offset voltage was typically varied between 0 V and 8 V and the ramp rate between 50 V ms^{-1} and 1600 V ms^{-1}. The latter allowed accounting for injection barrier effects.[51] The analysis was carried out following the diffusion-corrected eqn (11) of ref. 51 with saturation and geometric displacement current densities extracted from the CELIV curves.

Density functional theory calculations

Periodic DFT calculations on the *o*-IDTBR crystalline structure have been performed using the CASTEP module with Materials Studio software. All calculations have been carried out with the PBE GGA functional, a plane-wave energy cutoff of 50 Rydbergs (680 eV) and a *k*-point spacing of 0.05 Å^{-1}.[52] The crystalline structure of *o*-IDTBR has first been full relaxed using the Tkatchenko–Scheffler dispersion correction method, optimizing both all atomic positions within the cell and unit cell parameters. The resulting DFT-optimized cell parameters (a =

13.8706 Å, $b = 15.5913$ Å, $c = 32.6925$ Å, $\alpha = 90°$, $\beta = 96.0529$, and $\gamma = 90°$) are in excellent agreement with the measured crystallographic data in Table 1. NMR calculations have then been performed on the optimized crystal structure using the Gauge-Including Projector Augmented-Wave method (GIPAW); reference shieldings of 31.09 and 179.02 ppm were used for ^{1}H and ^{13}C, respectively.

Results and discussion

Structural analysis

A common way of classifying the organic semiconductor packing motif is by observing its π–π stacking dimensionality.[19,53–56] A–D–A molecules (Fig. 2) in particular can form highly interconnected domains through intermolecular interactions between the acceptor units (A units) of adjacent molecules.[19,57] The percolation pathway that forms through π–π stacking can develop along multiple directions of the crystalline domain. Molecules can arrange through a brickwork pattern with 2D percolation pathways, or through the so-called "reticular" packing motif which is characterised by 3D-interconnected domains. For herringbone crystal structures the molecular backbones of adjacent units are orthogonal and therefore lack π–π stacking (Fig. 1).

To reveal the NFA packing within the BHJ we started our investigations from single crystals, which represent the perfect platform to explore the influence of the solid-state arrangement on the charge transport. Most of the crystal structures analysed in this work were previously resolved by our group,[19] while others were found in the literature. As indicated in Table 1, some NFAs showed polymorphism. For instance, ITIC single crystals can be found to be either 0D herringbone or 2D brickwork motifs and *m*-4TICO also presents two different unit cells.

Single crystals represent the NFA molecular ordering of high purity and large millimetre sized crystals grown under controlled conditions (solvent vapour diffusion, see ref. [19]) and measured by XRD in a low-temperature (100 K) environment. Thus, it is possible to observe substantial differences in the molecular arrangement as we deviate from such ideal systems towards the BHJ. Therefore, we wanted to understand how the crystal packing changes by raising the temperature to ambient conditions (200 K shift between single crystals and powder XRD) and by disrupting the ideal growth conditions and long-range crystallinity of NFA single crystals. As an intermediate step, ss-NMR and XRD of purified NFA powder were performed. In the main text, we limit our observations on *o*-IDTBR, extending the analysis and discussion to the other materials in the ESI† (pages S6–S9).

From single crystals to powder

o-IDTBR has a 3D reticular packing motif in the single crystal,[58] characterised by close-contacts between the electron accepting units (A units) of tilted adjacent molecules (Fig. 1). To understand if this packing geometry is retained in powder samples, we performed X-ray diffraction and ss-NMR measurements. The powder diffractogram showed long-range crystallinity with well-defined Bragg peaks in the low-angle region (Fig. 3a). A partial agreement exists between the experimental data and the simulated 1D pattern of the single crystal structure, yet a certain mismatch between the positions for most of the reflections suggests that a slightly different unit cell is formed in powder. This can occur because of the temperature shift (200 K) between the single crystal and powder XRD measurements,‖ which can impact the long-range order, the local structures and packing interactions. In a first approximation,** we manually solved the reciprocal-space metric tensor equation for monoclinic structures[59] to derive the lattice parameters from the experimental data (Table S1†). The spectral agreement between the "manually-refined" simulated diffractogram and the experimental data improves (Fig. 3a), as the Goodness of Fit (GOF), Chi2 and residuals (wR) parameters are now reduced. This means that a better fit is obtained after the manual refinement, and therefore it is reasonable to assume a structural agreement between the two phases. A further confirmation is obtained when the lattice parameters and unit cell angles are derived through Le Bail refinement, suggesting that the structure undergoes a volumetric expansion from the single crystal to the powder phase (Table S1†), possibly resulting from the different temperatures of the measurements (see ESI, Fig. S5 and Table S2†) causing subtle changes in the local interactions.

To further confirm this behaviour, we performed NMR crystallography analysis, which combines XRD, ssNMR spectroscopy and modelling (here first principles calculations and GIPAW-DFT based NMR chemical shielding calculations) techniques to resolve atomic-scale interactions.[60] Solid-state NMR is particularly sensitive to the local structures of polymeric organic semiconductors, NFAs and polymer:NFA blends.[61–63] Here, we carried out ssNMR crystallography analysis with the aim of identifying the changes in local structures in crystals and powder compositions (Fig. 3b–d). This is achieved by analysing and comparing the ^{1}H and ^{13}C chemical shifts of crystal structures as calculated by the GIPAW-DFT approach with the experimentally measured ^{13}C and ^{1}H chemical shifts for the *o*-IDTBR powder. A detailed analysis of experimental 1D ^{1}H, ^{13}C and 2D ^{1}H–^{1}H and ^{1}H–^{13}C correlation ssNMR spectra is presented in the ESI (Fig. S1–S4†). Periodic DFT optimised crystal structures are shown in Fig. 3c, whereby the backbone–backbone and backbone–sidechain interactions are indicated by soft-rectangles (in red) and circles (in blue), respectively. Fig. 3b and d compare the 2D plots of DFT-calculated chemical shifts generated by MagresView and MagresPython software tools[64] for ^{1}H–^{1}H and ^{1}H–^{13}C spin pairs within a 3 Å distance, overlaid on the experimental ^{1}H–^{1}H double-quantum–single-quantum (DQ–SQ) correlation and ^{1}H–^{13}C nuclear correlation spectra. In 2D NMR measurements of this type, 2D peaks corresponding to ^{1}H–^{1}H and ^{1}H–^{13}C proximities within sub-nanometre distances in powder solids are detected. It is noteworthy that a good correlation between the GIPAW-DFT calculated chemical

‖ Single crystal structures are measured under a continuous flow produced by liquid nitrogen at 100 K, while powder diffraction is measured at 300 K.

** We assume in this first step that the unit cell angles (α, β and γ) are not varying from the single crystal unit cell.

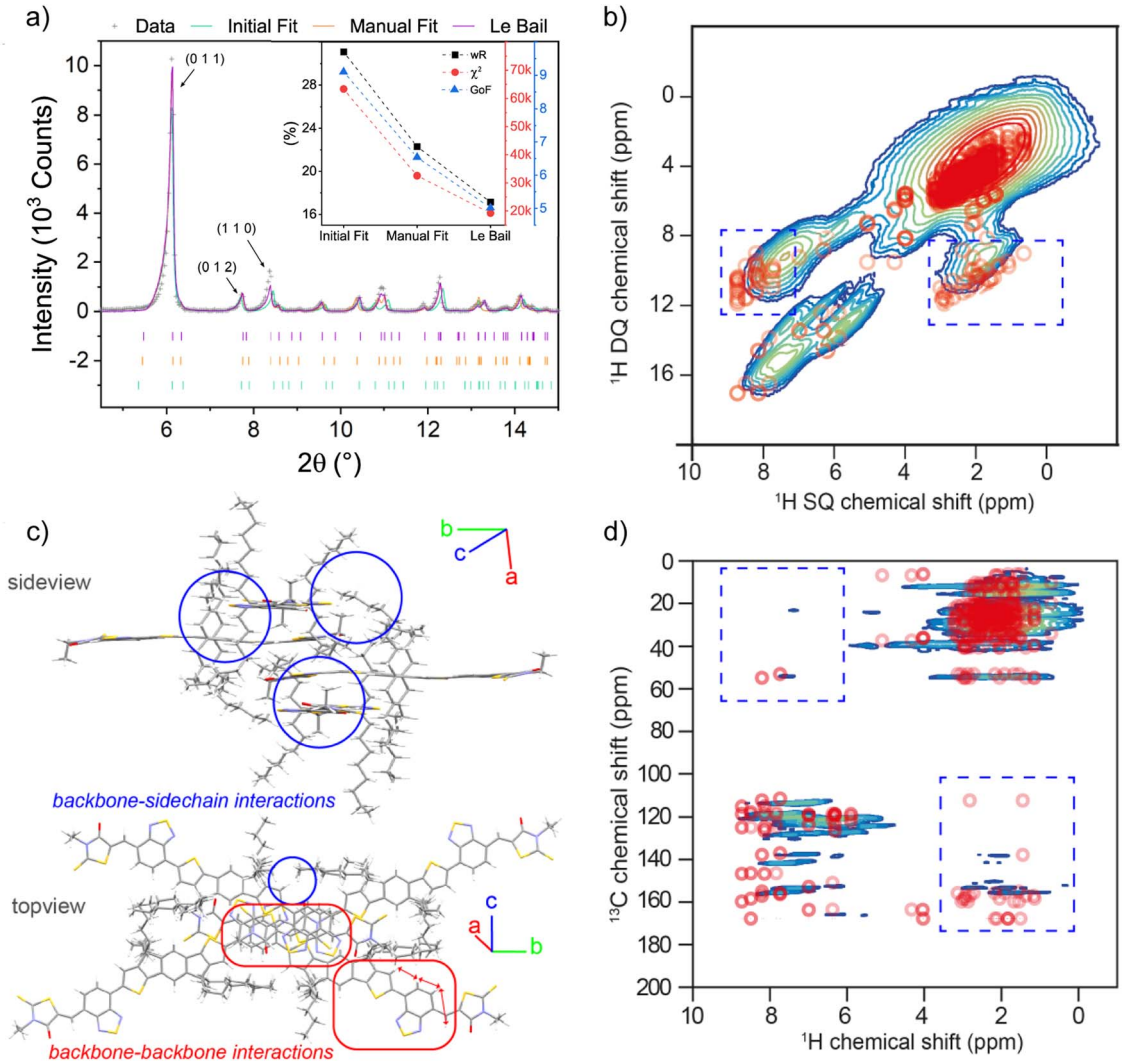

Fig. 3 (a) Powder XRD diffractogram overlaid with the simulated powder pattern of the single crystal structure. The inset shows the progressive improvement of the fitting from the original fit to manual and Le Bail refinement. (c) Periodic DFT optimised crystal structure and highlighted backbone–backbone (red boxes) and backbone–sidechain interaction (blue boxes). (b–d) DFT calculated 2D plots of the ^{1}H–^{1}H and ^{1}H–^{13}C chemical shifts (red circles) overlaid on the experimental ^{1}H–^{1}H double-quantum–single-quantum (DQ–SQ) correlation and ^{1}H–^{13}C heteronuclear correlation spectra (contours), respectively. The dashed blue rectangles indicate the minor changes in the backbone–sidechain interactions when comparing the crystalline to the powder form, meaning that the π–π interactions (along with the packing motif) remain substantially unvaried.

shifts and the experimental chemical shifts (δ) is observed for both aliphatic and aromatic moieties. In the DQ–SQ spectrum (Fig. 3b), the broad DQ peak at 0–8 ppm on the vertical axis is due to the ^{1}H–^{1}H proximities in alkyl sidechains and the DQ peaks in the 12–16 ppm range are due to the through-space ^{1}H–^{1}H proximities between aromatic groups within the chain and in between the π–π stacked *o*-IDTBR molecules, both of which exhibit good agreement with the DFT-calculated chemical shifts. However, subtle differences between the DFT calculated and experimental chemical shifts δ ($^{1}H_{DQ}$) in the 8–12 ppm range (dashed blue boxes), which originate from through-space dipolar interactions between aromatic groups and sidechains, indicate minor changes in the backbone–sidechain interactions in the vicinity of CH_2 moieties when comparing the crystalline and powder forms.[65] Similarly, a good agreement is obtained when comparing the DFT-calculated chemical shifts of ^{1}H–^{13}C pairs with the experimental ^{1}H–^{13}C 2D peaks in the HETCOR spectrum, which shows 2D peaks associated with the sidechains at δ (^{13}C) = 10–40 ppm and δ (^{1}H) = 1–4 ppm, and the backbone moieties δ (^{13}C) = 110–170 ppm and δ (^{1}H) = 5–9 ppm (Fig. 3d). However, deviations between the DFT-calculated *versus* experimental chemical shifts are observed for the 2D peaks corresponding to the through-space aromatic-sidechain dipolar interactions as depicted in the blue dashed boxes. Similar trends are observed for Y-series NFAs that showed changes in the local structures with respect to the backbone–sidechain interactions between the crystalline and powder forms.[60] The most important take away from the ssNMR crystallography study is that it allowed us to leverage the Le Bail refinement as a tool to verify the structural compatibility

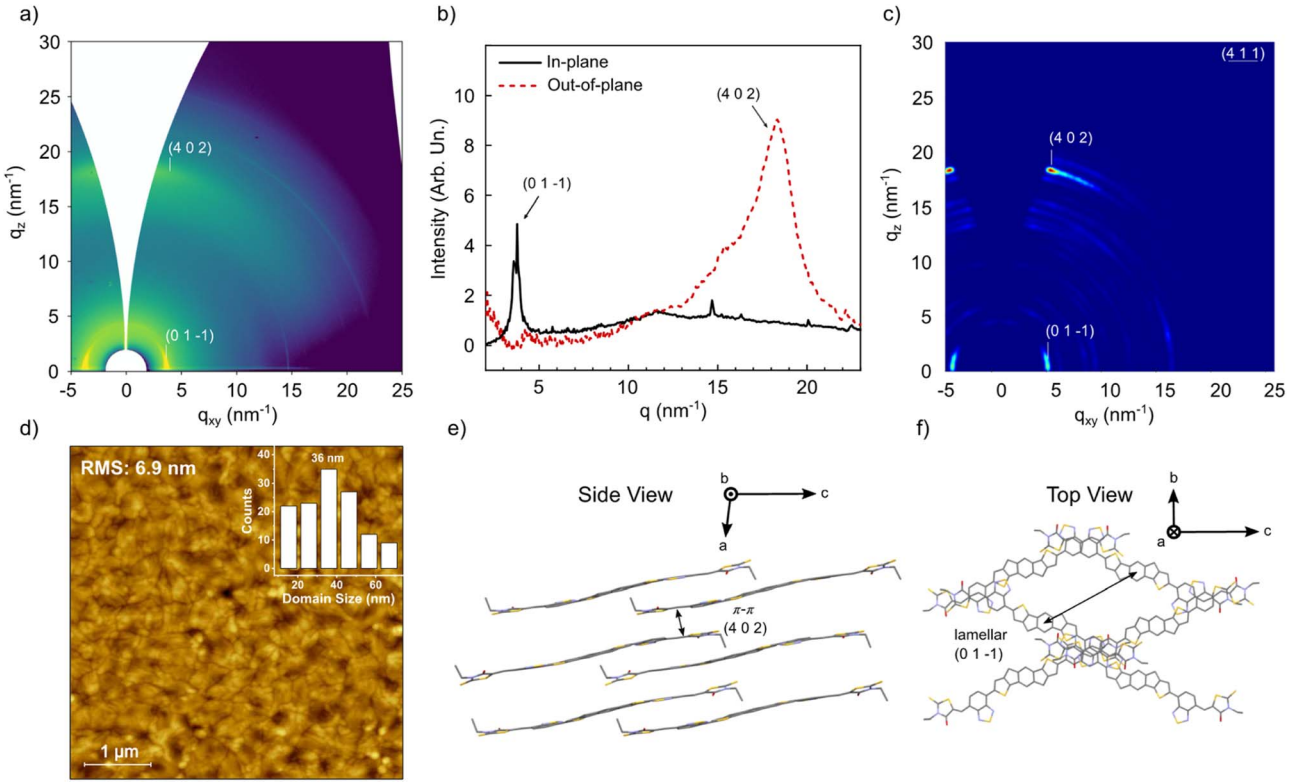

Fig. 4 *o*-IDTBR GIWAXS pattern (a) with in-plane and out-of-plane integration profiles along $q_z \sim 0$ and $q_{xy} \sim 0$, respectively. (b). Simulated GIWAXS pattern of the *o*-IDTBR unit cell oriented along the (4 1 1) direction. The good agreement with the experimental GIWAXS confirmed a face-on 3D reticular packing motif of *o*-IDTBR in the blend. (c). 5 × 5 μm AFM image (d) of the *o*-IDTBR film with the domain size distribution and average value (inset). Side (e) and top (f) views of the *o*-IDTBR crystal packing with π–π stacking (4 0 2) and lamellar (0 1 –1) peaks.

between single crystal and powder forms in terms of packing motif. This is possible as it allows for shift in the lattice parameters caused by side chain relaxation at elevated temperatures and demonstrated by changes in the backbone–sidechain interactions, while preserving the π–π interactions. By extending the Le Bail analysis to the other NFAs of interest (Fig. S5–S8 and Table S3†), we obtained useful information about the material crystallinity:

(1) The ITIC herringbone polymorph is predominant over the brickwork (Fig. S7†).

(2) *m*-4TICO presents two brickwork structures but only the un-solvated one is represented in powder (Fig. S8†).

(3) *o*-IDTBR, IDIC, *m*-ITIC and 4TICO single crystal packing is preserved in powder (Fig. 3a and S6†).

(4) With the only exception of 4TIC,§§ all the NFAs show several Bragg peaks in the low angle region.

(5) All the non-solvated structures undergo a volumetric expansion due to the temperature difference between single crystal and powder experiments. However, we do not exclude that the volumetric reduction observed for the solvated crystals is only apparent, given that a significant volume portion in the single crystal structure is occupied by the solvent, which is not expected to be found in the powder structure.

§§ 4TIC powder XRD data quality didn't allow Le Bail analysis to be performed due to poor scattering (Fig. S6).

A summary of the results obtained by Le Bail refinement performed for the different NFAs can be found in Table S3.†

From powder to NFA films

A further intermediate step to approach the NFA packing in the BHJ was to study the molecular organisation in thin films. Here, we expected to see a more compatible unit cell to the one observed in powder rather than in single crystals as we were going towards systems that are presumably composed of many little crystallites with reduced long-range order, cumulative disorder and multiple orientations.[35] Moreover, the temperature held during GIWAXS measurements on the film was 300 K as for the powder experiments (XRD and ss-NMR). For convenience, we here report the analysis performed on *o*-IDTBR, while the complete dataset including the other materials can be found in the ESI† (pages S10–S19).

The GIWAXS data of the *o*-IDTBR film with related 1D integration profiles along the in-plane and out-of-plane directions are shown in Fig. 4a, b and Table 2. From the q-map two main contributions are visible: a low-angle component, located at $q \approx 3.8$ nm^{-1}, which is generally recognised as a lamellar peak and is indicative of the separation of the conjugated and aliphatic moieties,[36] and a higher angle feature ($q \approx 18.3$ nm^{-1}) which is commonly attributed to π–π stacking.[66] Given the anisotropic nature of these two main diffraction components, we expected

Table 2 Crystallographic information of the main peaks observed by GIWAXS on *o*-IDTBR, PBTZT-stat-BDTT-8 and PBTZT-stat-BDTT-8:*o*-IDTBR films. AFM domain size and purity are also shown. The domain purity parameter (ϕ) is defined as the ratio (in percent) between the CCL and the domain size obtained by AFM

Component	Peak	Orientation	q (nm^{-1})	d (nm)	FWHM (nm^{-1})	CCL (nm)	g	Domain Size (nm)	ϕ (%)
NFA film									
o-IDTBR	(0 1 −1)	In-plane	3.79	1.66	0.27	20.9	10.6	36 ± 7	58.1
o-IDTBR	(4 0 2)	Out-of-plane	18.35	0.34	2.22	2.5	13.9	—	—
Polymer film									
PBTZT-stat-BDTT-8	(1 0 0)	In-plane	2.71	2.32	0.78	7.2	21.4	24 ± 5	30.2
PBTZT-stat-BDTT-8	(0 1 0)	Out-of-plane	18.05	0.35	0.75	7.5	25.7	—	—
Blend film									
o-IDTBR	(0 1 −1)	In-plane	3.77	1.67	0.33	17.1	11.8	50 ± 10	34.3
PBTZT-stat-BDTT-8	(1 0 0)	In-plane	2.80	2.24	1.58	3.6	30.0	—	—
PBTZT-stat-BDTT-8, *o*-IDTBR	(0 1 0) + (4 0 2)	Out-of-plane	18.14	0.35	2.80	2.0	15.7	—	—

a π–π stacking with a preferential face-on crystalline orientation of the *o*-IDTBR domains. To validate our hypothesis, we simulated the GIWAXS pattern of the *o*-IDTBR single crystal structure (Le-Bail refined) oriented along the (4 1 1) direction (Fig. 4c), which is nearly parallel to the π–π stacking (4 0 2) and perpendicular to the lamellar (0 1 −1) peak (Fig. 4e). The good agreement between the simulated and experimental diffraction data suggests that the *o*-IDTBR packing motif is preserved in the film, where the domains adopt a face-on orientation with an in-plane lamellar ordering (0–1 1) and out-of-plane π–π stacking (4 0 2). The good agreement between our findings with the literature[67,68] clarifies the crystal packing motif and orientation of the *o*-IDTBR films.

Some more considerations on the *o*-IDTBR film crystallinity can be done by focussing on the spectral shape of the main diffraction peak (lamellar peak). According to the paracrystalline g parameter found for the lamellar peak (Table 2),[35] the film can be classified on the boundary between semi-paracrystalline and amorphous, showing a Crystal Coherence Length (CCL) of ~20 nm. For this class of materials, a direct quantification of the crystalline domain size from the CCL is often not possible. According to the nomenclature used in ref. 35, we will refer to the CCL as the spatial extent of the coherently diffracting regions included in the paracrystallites, *i.e.* column lengths.[35]

To access the NFA domain size (which can be composed of multiple paracrystallites), we investigated the surface morphology by AFM. Fig. 4d shows well-defined domain boundaries and a root mean square (RMS) roughness of 6.9 nm. We performed the AFM image segmentation (see pages S20–S25†) through the watershed algorithm to derive the average domain size and its distribution.[46] From the calculations, we observed an average domain size of 36 nm from the maximum of the peak distribution (inset of Fig. 4d and Table 2). This value is higher than the CCL, which confirmed that *o*-IDTBR domains (visible from the AFM) are composed of multiple paracrystallites, whose column length is determined by XRD (CCL). To get an indication of the domain structural purity, we introduced a parameter (ϕ) defined as the ratio (in percent) between the CCL and the domain size obtained by AFM (Table 2).

Analogue characterisation and analysis were performed on the other NFAs of interest for this work (Fig. S9–S14, Tables S4–S9†) and some key considerations and results can be summarised as follows:

(1) Most of the NFA films showed a well-defined GIWAXS scattering, especially in the lamellar and π–π stacking regions (Fig. S9–S12, Tables S4–S7†). These two main features are characterised by a low angular distribution and therefore are indicative of a preferential orientation of the crystalline domains with respect to the substrate.

(2) *o*-IDTBR, *m*-4TICO, 4TIC, *m*-ITIC and IDIC crystal lattice simulations yielded a good structural agreement with the powder unit cell obtained by Le Bail refinement (Fig. S9–S12a†). This proved that a structural continuity in terms of the packing motif occurs between powder and films.

(3) NFAs with 3D reticular (4TIC and *o*-IDTBR, see Fig. S9b†, 5e and f) and 2D brickwork (*m*-ITIC and IDIC, see Fig. S11–S12b†) crystal packing motifs are involved in a face-on domain orientation, with *m*-4TICO as the only exception ("quasi" edge-on crystal packing, see Fig. S10b†).

(4) ITIC and 4TICO were found to have a 0D-herringbone packing motif in powder. However, due to the lack of multiple Bragg peaks, texturing, and long-range crystallinity (Fig. S13, S14, Tables S8 and S9†), we could not perform any crystal lattice simulation. However, we do not exclude the presence of small and randomly oriented herringbone column lengths within the domains.

(5) The high g parameter found for all the NFAs (>9.5) prevented us from directly quantifying the crystallite domain size from the lamellar peak shape (FWHM) as the CCL represents the spatial extent of the coherently diffracting regions (Tables S4–S9†). We therefore estimated the domain size from AFM image segmentation along with an indication for the domain purity (ϕ).

(6) In general, NFAs that form π–π stacking structures (through 2D brickwork or 3D reticular motifs) in single crystals and powder showed the highest crystallinity in films (lowest g parameters and highest CCL, see Tables S4–S9†). Conversely, 0D herringbone NFAs (ITIC and 4TICO) provided the highest

paracrystalline parameter g, highest CCL, and surprisingly the highest domain purity ϕ.

NFAs blended with PBTZT-stat-BDTT-8

After having characterised the NFA film crystallinity, we extended our investigation on NFA:PBTZT-stat-BDTT-8 blend films, which were used as active layers for the solar cell fabrication (see below). As for the rest of the structural characterisation, we here limit the discussion on the PBTZT-stat-BDTT-8:*o*-IDTBR blend while the analysis for the other systems can be found in the ESI.†

The PBTZT-stat-BDTT-8 polymer GIWAXS pattern is shown in Fig. 5a, where a (1 0 0) lamellar reflection is located at $q \approx 2.7$ nm^{-1} and the (0 1 0) π–π stacking feature at $q \approx 18.0$ nm^{-1}. The integration profiles suggest a prevalent in-plane orientation of the (1 0 0) feature and an out-of-plane direction of (0 1 0) (Fig. 5c and f). A slight face-on crystalline orientation of PBTZT-stat-BDTT-8 was previously reported, along with its smooth surface morphology with low RMS (Fig. 5d).[37]

The GIWAXS data and 1D profiles of the PBTZT-stat-BDTT-8:*o*-IDTBR blend are shown in Fig. 5b. A broad π–π stacking feature is located at $q \approx 18.1$ nm^{-1} along the out-of-plane direction (Fig. 5d), which can arise from both the NFA and the polymer due to the spectral overlap in the q range. Therefore, we focus on the lamellar features of *o*-IDTBR and PBTZT-stat-BDTT-8 as indicative of the distinct material ordering in the blend given that they can be distinguished from the in-plane profiles (Fig. 5c). The *o*-IDTBR (0 1 −1) lamellar peak is located here at $q \approx 3.8$ nm^{-1}, meaning that the NFA crystalline ordering in the blend is preserved with a similar lattice spacing and crystal packing.

A remarkable difference is reported for the spectral shape of the NFA lamellar peak as it is characterised by an increased FWHM, indicating a reduced long-range ordering (lower CCL) of the *o*-IDTBR domains in the blend when compared to the pure *o*-IDTBR film, resulting in higher g. In addition to this, the increased domain size calculated from the AFM image (Fig. 5e) implies a lower degree of domain purity (φ) of the NFA in the blend (Table 2).

The analysis for the other NFAs can be found in the ESI† (Fig. S9–S14, Tables S4–S9). However, the main conclusions can be outlined as follows:

(1) The NFA crystallinity in PBTZT-stat-BDTT-8:NFA blends presented broader and slightly shifted (towards lower q) lamellar peaks. As a result, the NFA domains in the blend are characterised by reduced crystallinity (lower CCL and higher g) and relaxed lamellar packing with respect to the bare NFA film. Furthermore, the presence of the polymer also affects the

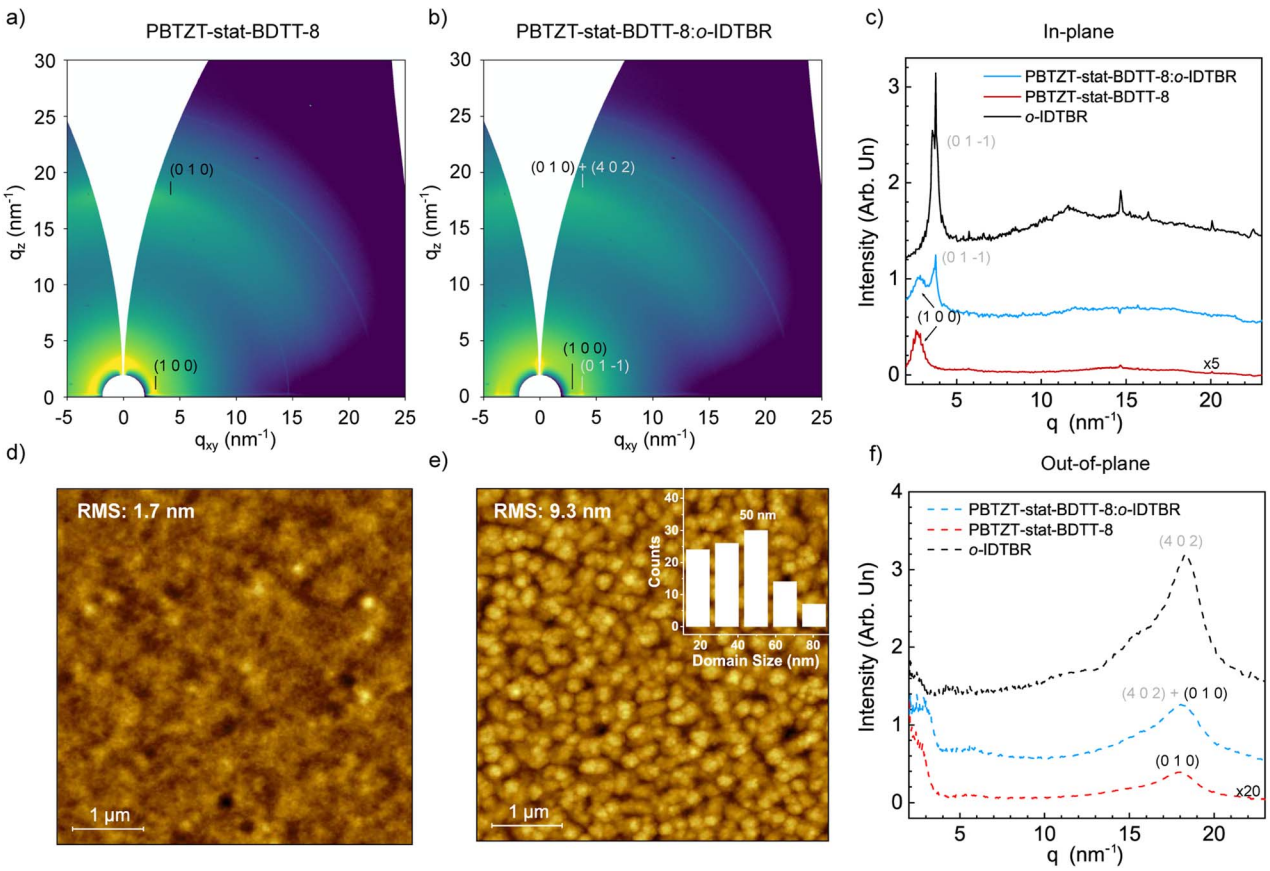

Fig. 5 PBTZT-stat-BDTT-8 (a) and PBTZT-stat-BDTT-8:*o*-IDTBR (b) GIWAXS patterns with in-plane (c) and out-of-plane (f) integration profiles. The NFA features are clearly visible from the blend GIWAXS, which confirmed that *o*-IDTBR maintains the packing motif in the blend. 5 × 5 μm AFM images of PBTZT-stat-BDTT-8 (d) and PBTZT-stat-BDTT-8:*o*-IDTBR (e) with the domain size distribution and average value (inset).

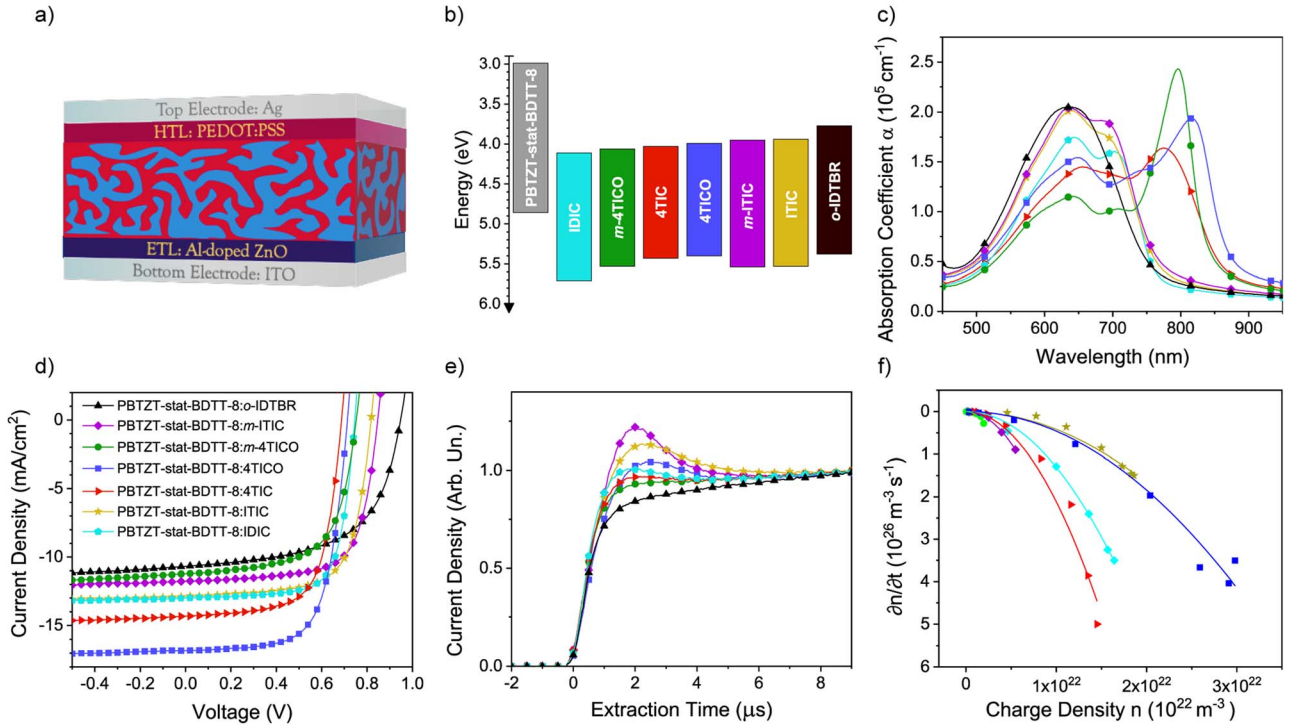

Fig. 6 Device architecture with 80 ± 5 nm thick active layers (a) and energy levels determined by Air Photoemission Spectroscopy (see the Experimental section) (b) of PBTZT-stat-BDTT-8 and the different NFAs used for the solar cells' fabrication. UV-vis of the different active layers (c). Characterisation of solar cells: *J*–*V* characteristics under illumination (dark curves are plotted in Fig. S17†) (d), photo-CELIV curves (e) and bimolecular recombination coefficients (f). Legends of panels (c–f) are shared and shown in (d).

domain purity (ϕ), which is reduced for most of the blends with respect to the films made of NFAs.

(2) NFAs with 3D-reticular (*o*-IDTBR and 4TIC) and 2D-brickwork (*m*-4TICO, IDIC and *m*-ITIC) arrangements in pure NFA films preserved their packing motif and texturing in NFA:PBTZT-stat-BDTT-8 blends (Fig. 5 and pages S10–S17†).

(3) NFAs that formed 0D herringbone structures in single crystal and powder phases (ITIC and 4TICO) showed the lowest crystallinity (highest *g* parameter and lowest CCL calculated on the NFA lamellar peak) and poor texturing among the series of NFA:PBTZT-stat-BDTT-8 blends (pages S18–S19†). Our results are in good agreement with a recent report, where the importance of the π–π stacking interaction energy to preserve the NFA packing motif in the blend films is highlighted.[69]

Solar cell characteristics

To investigate the role of the NFA packing motif and crystallinity on the charge transport properties and performance of OSCs, we fabricated inverted architecture devices (Fig. 6a). The NFAs of interest were tested with PBTZT-stat-BDTT-8 active layers and optimised with respect to the choice of the solvent, casting temperature, and post-annealing treatment (Table S10†). The energy levels of the different NFAs with respect to the donor polymer are shown in Fig. 6b, along with the UV-vis spectra of each active layer used (Fig. 6c). The *J*–*V* curves delivering the highest PCE are shown in Fig. 6d, and the *J*–*V* characteristics are listed in Table 3 (dark *J*–*V* curves in Fig. S24†). Surprisingly, 4TICO and ITIC were among the best performing NFAs in terms of maximum and average PCE obtained, despite having the lowest crystallinity as indicated by the highest *g* parameter and lowest CCL (Table 3). Moreover, the NFA crystal packing motif does not seem to have a direct impact on performance (Table 3): 3D reticular packing NFAs such as *o*-IDTBR and 4TIC reached a maximum PCE of 6.6 and 5.9 while *m*-4TICO (2D brickwork packing motif) was the least performing NFA (5.3% PCE). Interestingly, NFAs with a 0D herringbone packing motif in single crystals (4TICO and ITIC) delivered the highest performance (8.1% and 7.2%, respectively). Nevertheless, we still expected a strong interplay between the active layer crystallinity, NFA packing, and charge transport properties, which may have an impact on the solar cell performance and in particular the FF.[70,71] Thus, we performed photo-CELIV experiments to determine the charge mobility and the bimolecular recombination coefficient for each NFA:PBTZT-stat-BDTT-8 blend (Fig. 6e, f and Table 3)¶¶.[49,72–78]

With regards to the mobility, we observed a remarkable correlation between the NFA lamellar CCL in the blend and the charge mobility (Fig. 7a). The lowest mobility for ITIC and 4TICO blends is related to their poor crystallinity (low CCL and high *g* parameter) detected in the pure NFA (Tables S4–S9†) and

¶¶ We did not detect a meaningful signal from *o*-IDTBR:PBTZT-stat-BDTT-8 to extract the mobility and recombination coefficient. We believe that this is due to a combination of factors, among which the lowest shunt resistance leading to the lowest FF observed among all the different devices.

Table 3 Solar cell characteristics for the different NFAs combined with PBTZT-stat-BDTT-8. Results for the best solar cell in terms of PCE (average and standard deviation over a minimum of 10 devices) are shown for each active layer. Device mobility and bimolecular recombination coefficients are also listed along with the other parameters related to the film crystallinity (*g*, CCL, and packing), morphology (RMS and domain size) and domain purity (ϕ). The energy bandgap of the blend is also shown (E_g)

Active layer	PCE (%)	FF (%)	V_{OC} (mV)	J_{SC} (mA cm^{-2})	μ (cm^2 V^{-1} s^{-1})	β_{exp} (m^3 s^{-1})	*g*	CCL (nm)	Dom. size (nm)	φ (%)	RMS (nm)	Packing	E_g (meV)
PBTZT-stat-BDTT-8:4TICO	8.1 (7.5 ± 0.3)	70.9 (68.5 ± 1.2)	725 (717 ± 4)	16.8 (15.3 ± 0.7)	$5.2 \pm 0.5 \times 10^{-5}$	$4.6 \pm 2.3 \times 10^{-18}$	22.4	5.8	12.1 ± 2	47.7	1.4	0D	870
PBTZT-stat-BDTT-8:ITIC	7.2 (6.8 ± 0.2)	69.3 (67.5 ± 1.1)	820 (816 ± 3)	12.9 (12.4 ± 0.4)	$5.7 \pm 0.6 \times 10^{-5}$	$4.2 \pm 2.1 \times 10^{-18}$	21.0	5.7	9.6 ± 2	59.4	1.2	0D	920
PBTZT-stat-BDTT-8:IDIC	7.0 (6.8 ± 0.2)	73.0 (71.2 ± 1.7)	750 (745 ± 2)	13.4 (12.8 ± 0.4)	$1.4 \pm 0.1 \times 10^{-4}$	$1.3 \pm 0.6 \times 10^{-17}$	15.4	10.5	41.1 ± 8	25.5	5.1	2D	750
PBTZT-stat-BDTT-8:*m*-ITIC	6.9 (6.6 ± 0.3)	69.7 (67.7 ± 1.6)	850 (837 ± 7)	12.2 (11.7 ± 0.5)	$8.7 \pm 0.9 \times 10^{-5}$	$2.6 \pm 1.3 \times 10^{-17}$	16.3	8.4	51.5 ± 10	16.3	6.7	2D	910
PBTZT-stat-BDTT-8:4TIC	6.6 (6.4 ± 0.2)	67.5 (65.6 ± 1.1)	685 (685 ± 5)	14.3 (14.2 ± 0.3)	$1.1 \pm 0.1 \times 10^{-4}$	$2.1 \pm 1.0 \times 10^{-17}$	14.1	9.0	29.6 ± 6	30.3	2.7	3D	830
PBTZT-stat-BDTT-8:o-IDTBR	5.9 (5.6 ± 0.2)	58.7 (57.6 ± 0.6)	950 (944 ± 3)	10.8 (10.3 ± 0.4)	N/A	N/A	11.8	17.1	50.0 ± 10	34.3	10.1	3D	1090
PBTZT-stat-BDTT-8:*m*-4TICO	5.3 (4.6 ± 0.6)	63.7 (61.5 ± 1.6)	765 (755 ± 6)	11.2 (9.9 ± 1.1)	$1.4 \pm 0.1 \times 10^{-4}$	$1.2 \pm 0.6 \times 10^{-16}$	14.9	9.6	68.5 ± 14	14.0	11.7	2D	800

blend films (Table 3). The 0D packing nature might be another disadvantage for efficient long-range transport. The relationship between charge mobility and NFA crystallinity was further investigated by MIS-CELIV measurements, performed on electron-injecting devices. The electron mobility determined by MIS-CELIV matched the values obtained *via* photo-CELIV (Fig. S23†). Since the photo-CELIV current is dominated by the species with higher mobility,[79] we could attribute the photo-CELIV mobility to electrons. This leads to the conclusion that the electron mobility is clearly dependent on the NFA crystallinity, as expressed by the CCL and *g* parameter. However, the mobility determined from both photo-CELIV and MIS-CELIV did not dominate the solar cell performance, as seen from FF and PCE (Table 3). This result encouraged us to investigate the bimolecular recombination and its possible implications in the device performance.

We derived the bimolecular recombination coefficient by photo-CELIV, exploring a purely quadratic dependence between recombination and charge carrier density (Fig. 6f).[49] The model provided a good fit with the sweep-out of free charges at different time delays (Fig. 6f), and the bimolecular recombination coefficient (β_{exp}) was derived according to eqn (2) used in ref. 49 and is shown in Table 3. Interestingly, we find the lowest recombination coefficients for the solar cells made of ITIC and 4TICO blends, which delivered the highest performance and among the highest FF, highlighting the importance of the bimolecular recombination on the device parameters.[37,80] Despite their lower crystallinity, active layers made of ITIC and 4TICO resulted in higher domain purity (ϕ). Conversely, NFAs characterised by higher CCL and lower *g*, such as IDIC and *m*-4TICO, provided the lowest domain purity and highest bimolecular recombination coefficient. Overall, a correlation is found between the NFA domain purity and the bimolecular recombination coefficient (Fig. 7b). As mentioned above, the ϕ-parameter compares the spatial extent of the NFA ordered regions in the domain (*i.e.*, column lengths, derived from the CCL), with the domain size obtained from AFM images and can be calculated as follows: $\phi = \text{CCL (nm)}/\text{domain size (nm)} \times 100$. A blend film with low domain purity (ϕ) can be understood as formed by domains with a larger relative fraction of regions with an amorphous or mixed nature that prompt recombination.[81] Assessing domain purity *via* the ϕ-parameter is easy-to-access compared to more sophisticated methods such as resonant soft X-ray scattering (RSoXS).[82,83] To summarise the influence of the NFA crystallinity (*g*, CCL), packing motif and morphology (domain size, RMS and ϕ) on the solar cell parameters (PCE,†† FF, V_{OC} and J_{SC}) and charge transport properties (μ and β_{exp}), we built a multivariable cross-correlation map with the most relevant parameters‡‡(Fig. 8). While, strictly speaking, the cross-correlation map tests for linear correlation, data that are correlated in a non-linear

†† Although the PCE is a linear combination of FF, V_{OC} and J_{SC}, we included it in the cross-correlation analysis for convenience.

‡‡ We assigned a constant value for each motif which is representative of the dimensionality of the π–π stacking: "0" for 0D herringbone, "2" for 2D brickwork and "3" for 3D reticular.

fashion will still result in high (absolute) values. As such the map may serve as a semi-quantitative tool to assess correlations in complex multivariable systems, where not all dependencies are fully understood physically.

With regards to the initial motivation of our study on the role of the NFA crystal packing, we didn't observe a clear correlation with the device performance parameters. However, an enhanced propensity for NFAs with increasing directionality of π–π stacking to form crystalline domains in the blend is evident from the high Pearson correlation coefficient (r) between the packing motif with g and CCL, 0.97 and 0.76, respectively. Thus, the directionality of the π–π stacking directly promotes the NFA

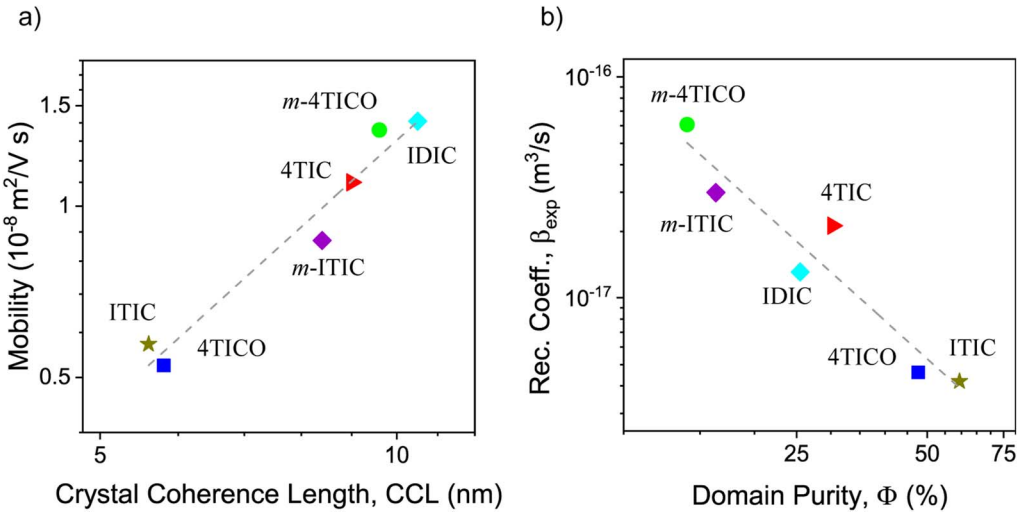

Fig. 7 (a) Mobility is plotted *versus* the NFA crystal coherence length in the blend films. A linear fit of the data is represented with a dashed grey line and indicates a correlation between CCL and electron mobility. (b) Bimolecular recombination coefficient determined by photo-CELIV in relation to the NFA domain structural coherency in the blend. A linear fit is represented with a dashed grey line and indicates a correlation between the bimolecular recombination coefficient and the domain purity.

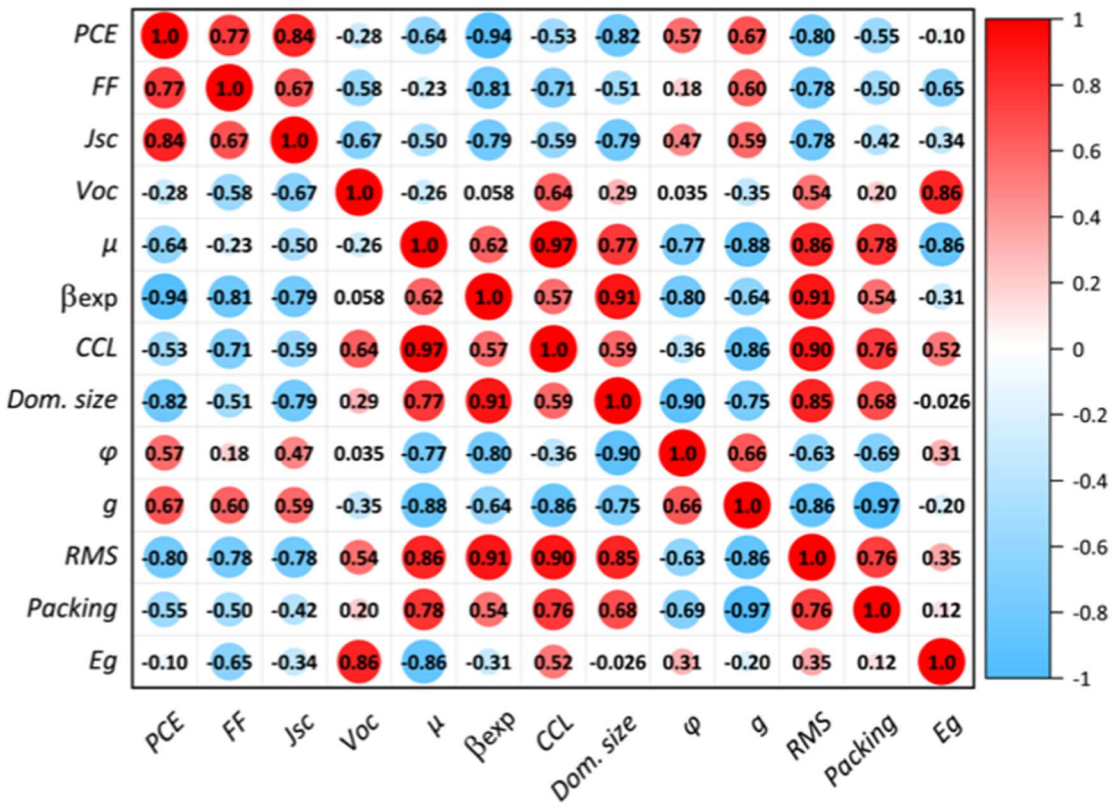

Fig. 8 Multivariable cross-correlation map between solar cell characteristics and crystallinity/morphology parameters.

crystallinity in blends (g and CCL), which , in turn, favours the electron mobility (the r coefficient of μ is 0.97 and −0.88 with CCL and g). It is worth mentioning that in a recent study, a long exciton diffusion lifetime was observed in systems with enhanced π–π stacking systems and crystallinity.[69] The tendence to obtain higher mobilities in organic solar cells by increasing the material crystallinity is generally acknowledged.[35,84–86] In addition to this, a lack of a direct correlation between the packing motif and performance was also reported.[69]

Interestingly, we found that the bulk heterojunction morphology has a bigger impact on performance. In particular, active layers forming big domains at the surface have low domain purity ($r = -0.9$), which is a good correlator for the bimolecular recombination coefficient (Fig. 7b, 8 and S25†). β_{exp} is, in turn, a first-tier correlator to J_{SC} and FF (r is −0.79 and −0.81, respectively) and the best correlating factor for the solar cell performance ($r = 0.94$). The primary importance of the bimolecular recombination for the device performance and its relationship with the domain purity was also observed in the literature.[87]

Among the selected factors included in the cross-correlation analysis, V_{OC} is generally not dependent on the film crystallinity and morphology. The energy bandgap of the blend E_G, determined from the difference between the HOMO of the polymer and the LUMO of the NFA (Fig. 6b), is the only significant correlator to $V_{OC.}$ The last result agrees with the general knowledge about the relationship between V_{OC} and the energetics of the donor and the acceptor used in the blend,[88–90] although other factors affecting the V_{OC} (such as radiative and non-radiative losses[90,91]) have been excluded from our calculations.

Conclusions

We have studied how NFA crystal packing evolves from single crystals to the bulk heterojunction of a solar cell. Given the complexity of unambiguously determining the NFA packing motif in an active layer, arising when moving from ideal systems, *i.e.*, millimetre-size single crystals, to the most complex BHJ morphology, we employed a step-by-step structural analysis. The first step involved ss-NMR crystallography and powder XRD, which helped us to leverage the Le Bail refinement as a quick and effective tool to verify the structural compatibility between single crystal and powder samples. Then, we combined GIWAXS, crystal lattice simulations and AFM to systematically identify the NFA packing motif in the bare NFA films and blends with the PBTZT-stat-BDTT-8 polymer and to derive key parameters to describe the material crystallinity (CCL and g parameter) and morphology (RMS, domain size and domain purity, ϕ). Finally, we investigated the influence of those key structural parameters on the solar cell performance and charge transport properties.

Our main findings are:

(1) NFA packing motifs largely track from single crystals to the thin-film blend.

(2) Compounds that crystallise easily as single crystals also show high crystallinity in the blend films. For instance, we found that the poor propensity of ITIC to form single crystals (as indicated by the multiple unsuccessful trials to grow single crystals)[19] also translates into a low blend crystallinity (high g and low CCL).

(3) NFAs with higher π–π stacking dimensionality showed an increased propensity to form crystalline films (low g and high CCL) in both NFA films and blends.

(4) Despite our initial expectations, the NFA packing motif does not directly correlate with the solar cell performance parameters.

(5) NFAs with high film crystallinity (low g and high CCL) provided higher electron mobility. However, the mobility is not the dominating factor for device performance. At the same time, we found no correlation between the NFA crystallinity in the blend and the bimolecular recombination coefficient (β_{exp}).

(6) The bimolecular recombination coefficient (β_{exp}) is found to be the main factor influencing FF and J_{SC}. Systems with low β_{exp} reported the highest performance. For instance, the blend with lower NFA crystallinity (4TICO and ITIC) delivered the highest performance and lowest bimolecular recombination despite the lowest electron mobility.

(7) Domain purity stood out as an interesting design target, to limit the bimolecular recombination and obtain high efficiencies in organic solar cells. A better understanding of the influence of molecular properties on domain purity is needed.

A high domain purity could be targeted through a chemical design that aims at limiting void space within the unit cell while also managing the solubility/miscibility of the donor–acceptor pairing to control BHJ formation and intermolecular interactions.[37,92] This could in theory be targeted by the design of space filling yet flexible sidechains to increase the NFA rotational freedom and prevent NFA crystallisation that might induce an excessive phase segregation.[38] Alternatively, thermal annealing can also be used as a handle to tune the morphology of kinetically trapped systems,[93,94] allowing the formation of a controlled BHJ morphology characterised by the domain with high structural purity.[37,93,95] This was observed for NFAs that can rearrange their structures undergoing an endothermic transition (glass or liquid crystalline) during the post-annealing process (ITIC and 4TICO). Conversely, systems with shorter or sterically locked sidechains may promote the formation of crystalline domains even before any thermal treatment (4TIC, *m*-4TICO, and *m*-ITIC).[37] These domains tend to excessively phase segregate upon annealing without improving their domain purity.

Author contributions

P. Mondelli has prepared all the samples and performed XRD, GIWAXS, air photoemission spectroscopy and UV-vis experiments, fabricated, optimised and characterised the solar cells by J–V measurements and photo-CELIV, fabricated the electron only devices for MIS-CELIV and wrote the manuscript. P. Kaienburg has performed MIS-CELIV experiments and supported the discussion of the results. F. Silvestri has performed

AFM experiments and provided support for the 2D-GIWAXS experiments. R. Scatena has supported some of the XRD experiments and the discussion of the results. C. Welton has performed the ss-NMR characterisation. G. N. M. Reddy has supervised the ss-NMR experiments. M. Grandjean has contributed to the solar cell fabrication and optimisation. V. Lemaur has performed GIPAW calculations. E. Solano has supervised the 2D-GIWAXS experiments and contributed to the related data analysis. M. Nyman has supervised the MIS-CELIV characterisation. P. Horton and S. Coles have supported some of the XRD experiments. E. Barrena has supervised the 2D-GIWAXS and AFM characterisation. M. Riede, P. Radaelli, D. Beljonne and G. Morse have supported the discussion of the results and evaluated the manuscript. G. Morse has supervised the project.

Conflicts of interest

Merck KGaA provided the PBTZT-stat-BDTT-8 polymer and the 4TICO NFA.

Acknowledgements

P. Mondelli, F. Silvestri, E. Barrena and M. Riede acknowledge the European Union's Horizon 2020 research and innovation programme under Marie Skłodowska Curie Grant agreement no. 722651 (SEPOMO) for the support in the realization of this work. P. Kaienburg acknowledges funding from the Global Challenges Research Fund (GCRF) through STFC, START project ST/R002754/1; and from EPSRC for a Postdoctoral Fellowship EP/V035770/1. GIWAXS experiments were performed at the NCD-SWEET beamline at the ALBA synchrotron with the collaboration of ALBA staff (proposal 2019093873). M. Nyman acknowledges funding from the Academy of Finland through project #326000. M. Reddy acknowledges European Union's Horizon 2020 Research and Innovation Programme under the Skłodowska-Curie Grant (No. 79529). ss-NMR experiments were performed at the large-scale NMR facilities cofounded by IR INFRANALYTICS FR-2040. E. Barrena acknowledges funding by the Spanish Ministry under project PID2019-110907GB-I00 (AEI/FEDER, UE). P. Mondelli acknowledges support under the European Union's Horizon 2020 research and innovation programme "GREENELIT", Grant Agreement No. 951747.

References

1 L. Zhu, M. Zhang, J. Xu, C. Li, J. Yan, G. Zhou, W. Zhong, T. Hao, J. Song and X. Xue, *Nat. Mater.*, 2022, **21**, 656–663.
2 Y. Cui, Y. Xu, H. Yao, P. Bi, L. Hong, J. Zhang, Y. Zu, T. Zhang, J. Qin and J. Ren, *Adv. Mater.*, 2021, **33**, 2102420.
3 S. Li, C.-Z. Li, M. Shi and H. Chen, *ACS Energy Lett.*, 2020, **5**, 1554–1567.
4 Q. Wei, W. Liu, M. Leclerc, J. Yuan, H. Chen and Y. Zou, *Sci. China: Chem.*, 2020, 1–15.
5 J. Yuan, Y. Zhang, L. Zhou, G. Zhang, H.-L. Yip, T.-K. Lau, X. Lu, C. Zhu, H. Peng, P. A. Johnson, M. Leclerc, Y. Cao, J. Ulanski, Y. Li and Y. Zou, *Joule*, 2019, **3**, 1–12.
6 H. Lai, Q. Zhao, Z. Chen, H. Chen, P. Chao, Y. Zhu, Y. Lang, N. Zhen, D. Mo and Y. Zhang, *Joule*, 2020, **4**, 688–700.
7 G. Li, X. Zhang, L. O. Jones, J. M. Alzola, S. Mukherjee, L.-w. Feng, W. Zhu, C. L. Stern, W. Huang and J. Yu, *J. Am. Chem. Soc.*, 2021, **143**, 6123–6139.
8 L. Wang, Q. An, L. Yan, H.-R. Bai, M. Jiang, A. Mahmood, C. Yang, H. Zhi and J.-L. Wang, *Energy Environ. Sci.*, 2022, **15**, 320–333.
9 L. Zhu, M. Zhang, G. Zhou, T. Hao, J. Xu, J. Wang, C. Qiu, N. Prine, J. Ali and W. Feng, *Adv. Energy Mater.*, 2020, **10**, 1904234.
10 L. Zhu, M. Zhang, W. Zhong, S. Leng, G. Zhou, Y. Zou, X. Su, H. Ding, P. Gu, F. Liu and Y. Zhang, *Energy Environ. Sci.*, 2021, **14**, 4341–4357.
11 S. S. Babu, H. Möhwald and T. Nakanishi, *Chem. Soc. Rev.*, 2010, **39**, 4021–4035.
12 F. Steiner, S. Foster, A. Losquin, J. Labram, T. D. Anthopoulos, J. M. Frost and J. Nelson, *Mater. Horiz.*, 2015, **2**, 113–119.
13 F. Lin, K. Jiang, W. Kaminsky, Z. Zhu and A. K.-Y. Jen, *J. Am. Chem. Soc.*, 2020, **142**, 15246–15251.
14 W. Zhu, A. P. Spencer, S. Mukherjee, J. M. Alzola, V. K. Sangwan, S. H. Amsterdam, S. M. Swick, L. O. Jones, M. C. Heiber and A. A. Herzing, *J. Am. Chem. Soc.*, 2020, **142**, 14532–14547.
15 G. Zhang, X.-K. Chen, J. Xiao, P. C. Chow, M. Ren, G. Kupgan, X. Jiao, C. C. Chan, X. Du and R. Xia, *Nat. Commun.*, 2020, **11**, 1–10.
16 S. Dai, M. Li, J. Xin, G. Lu, P. Xue, Y. Zhao, Y. Liu, M. Sun, L. Yu and Z. Tang, *J. Mater. Chem. A*, 2022, **10**, 1948–1955.
17 X. Wang, H. Lu, Y. Liu, A. Zhang, N. Yu, H. Wang, S. Li, Y. Zhou, X. Xu and Z. Tang, *Adv. Energy Mater.*, 2021, **11**, 2102591.
18 C. Li, J. Zhou, J. Song, J. Xu, H. Zhang, X. Zhang, J. Guo, L. Zhu, D. Wei and G. Han, *Nat. Energy*, 2021, **6**, 605–613.
19 P. Mondelli, G. Boschetto, P. N. Horton, P. Tiwana, C.-K. Skylaris, S. J. Coles, M. Krompiec and G. Morse, *Mater. Horiz.*, 2020, **7**, 1062–1072.
20 X. Shi, L. Zuo, S. B. Jo, K. Gao, F. Lin, F. Liu and A. K. Y. Jen, *Chem. Mater.*, 2017, **29**, 8369–8376.
21 T. J. Aldrich, M. Matta, W. Zhu, S. M. Swick, C. L. Stern, G. C. Schatz, A. Facchetti, F. S. Melkonyan and T. J. Marks, *J. Am. Chem. Soc.*, 2019, **141**(7), 3274–3287.
22 J. Qu, H. Chen, J. Zhou, H. Lai, T. Liu, P. Chao, D. Li, Z. Xie, F. He and Y. Ma, *ACS Appl. Mater. Interfaces*, 2018, **10**, 39992–40000.
23 S. M. Swick, W. Zhu, M. Matta, T. J. Aldrich, A. Harbuzaru, J. T. Lopez Navarrete, R. Ponce Ortiz, K. L. Kohlstedt, G. C. Schatz, A. Facchetti, F. S. Melkonyan and T. J. Marks, *Proc. Natl. Acad. Sci. U. S. A.*, 2018, **115**(36), E8341–E8348.
24 M. Wu, J. Zhou, Y. Luo, N. Zheng, C. Wang, L. Liu, Z. Xie and Y. Ma, *Org. Chem. Front.*, 2018, **5**(22), 3324–3330.

25 D. Yan, W. Liu, J. Yao and C. Zhan, *Adv. Energy Mater.*, 2018, 1800204, DOI: 10.1002/aenm.201800204.
26 S. Li, L. Zhan, W. Zhao, S. Zhang, B. Ali, Z. Fu, T.-K. Lau, X. Lu, M. Shi, C.-Z. Li, J. Hou and H. Chen, *J. Mater. Chem. A*, 2018, **6**, 12132–12141.
27 H. Lai, H. Chen, J. Zhou, J. Qu, P. Chao, T. Liu, X. Chang, N. Zheng, Z. Xie and F. He, *iScience*, 2019, **17**, 302–314.
28 Y. Zhang, Z. Liu, T. Shan, Y. Wang, L. Zhu, T. Li, F. Liu and H. Zhong, *Mater. Chem. Front.*, 2020, **4**, 2462–2471.
29 D. Mo, H. Chen, J. Zhou, N. Tang, L. Han, Y. Zhu, P. Chao, H. Lai, Z. Xie and F. He, *J. Mater. Chem. A*, 2020, **8**, 8903–8912.
30 X. Li, H. Huang, I. Angunawela, J. Zhou, J. Du, A. Liebman-Pelaez, C. Zhu, Z. Zhang, L. Meng and Z. Xie, *Adv. Funct. Mater.*, 2020, **30**, 1906855.
31 S. Feng, M. Li, N. Tang, X. Wang, H. Huang, G. Ran, Y. Liu, Z. Xie, W. Zhang and Z. Bo, *ACS Appl. Mater. Interfaces*, 2020, **12**, 4638–4648.
32 L. Ma, S. Zhang and J. Hou, *J. Mater. Chem. A*, 2023, **11**, 481–494.
33 H. Lai and F. He, *Adv. Energy Mater.*, 2020, **10**, 2002678.
34 Y. Xiao and X. Lu, *Mater. Today Nano*, 2019, 100030.
35 Z. Peng, L. Ye and H. Ade, *Mater. Horiz.*, 2022, **9**, 577–606.
36 Y.-Y. Lai, V.-H. Huang, H.-T. Lee and H.-R. Yang, *ACS Omega*, 2018, **3**, 18656–18662.
37 P. Mondelli, F. Silvestri, L. Ciammaruchi, E. Solano, E. Beltrán-Gracia, E. Barrena, M. Riede and G. Morse, *J. Mater. Chem. A*, 2021, **9**, 26917–26928.
38 S. Marina, A. D. Scaccabarozzi, E. Gutierrez-Fernandez, E. Solano, A. Khirbat, L. Ciammaruchi, A. Iturrospe, A. Balzer, L. Yu and E. Gabirondo, *Adv. Funct. Mater.*, 2021, 2103784.
39 H. Yoshida and N. Sato, *Appl. Phys. Lett.*, 2006, **89**, 101919.
40 G. Ashiotis, A. Deschildre, Z. Nawaz, J. P. Wright, D. Karkoulis, F. E. Picca and J. Kieffer, *J. Appl. Crystallogr.*, 2015, **48**, 510–519.
41 D. W. Breiby, O. Bunk, J. W. Andreasen, H. T. Lemke and M. M. Nielsen, *J. Appl. Crystallogr.*, 2008, **41**, 262–271.
42 L. Ye, K. Weng, J. Xu, X. Du, S. Chandrabose, K. Chen, J. Zhou, G. Han, S. Tan and Z. Xie, *Nat. Commun.*, 2020, **11**, 1–9.
43 C. F. Macrae, I. Sovago, S. J. Cottrell, P. T. Galek, P. McCabe, E. Pidcock, M. Platings, G. P. Shields, J. S. Stevens and M. Towler, *J. Appl. Crystallogr.*, 2020, **53**, 226–235.
44 G. M. Reddy, M. Malon, A. Marsh, Y. Nishiyama and S. P. Brown, *Anal. Chem.*, 2016, **88**, 11412–11419.
45 D. Nečas and P. Klapetek, *Open Phys.*, 2012, **10**, 181–188.
46 A. S. Kornilov and I. V. Safonov, *J. Imaging*, 2018, **4**, 123.
47 S. Berny, N. Blouin, A. Distler, H. J. Egelhaaf, M. Krompiec, A. Lohr, O. R. Lozman, G. E. Morse, L. Nanson, A. Pron, T. Sauermann, N. Seidler, S. Tierney, P. Tiwana, M. Wagner and H. Wilson, *Adv. Sci.*, 2016, **3**, 1500342.
48 J. Lorrmann, B. H. Badada, O. Inganäs, V. Dyakonov and C. Deibel, *J. Appl. Phys.*, 2010, **108**, 113705.
49 T. M. Clarke, C. Lungenschmied, J. Peet, N. Drolet and A. J. Mozer, *Adv. Energy Mater.*, 2015, **5**, 1401345.
50 G. Juška, N. Nekrašas and K. Genevičius, *J. Non-Cryst. Solids*, 2012, **358**, 748–750.
51 O. J. Sandberg, M. Nyman, S. Dahlström, S. Sandén, B. Törngren, J.-H. Smått and R. Österbacka, *Appl. Phys. Lett.*, 2017, **110**, 153504.
52 S. R. Chaudhari, J. M. Griffin, K. Broch, A. Lesage, V. Lemaur, D. Dudenko, Y. Olivier, H. Sirringhaus, L. Emsley and C. P. Grey, *Chem. Sci.*, 2017, **8**, 3126–3136.
53 C. Wang, H. Dong, L. Jiang and W. Hu, *Chem. Soc. Rev.*, 2018, **47**, 422–500.
54 M. Mas-Torrent and C. Rovira, *Chem. Rev.*, 2011, **111**, 4833–4856.
55 C. Wang, H. Dong, W. Hu, Y. Liu and D. Zhu, *Chem. Rev.*, 2011, **112**, 2208–2267.
56 C. Wang, H. Dong, H. Li, H. Zhao, Q. Meng and W. Hu, *Cryst. Growth Des.*, 2010, **10**, 4155–4160.
57 J. Hou, O. Inganäs, R. H. Friend and F. Gao, *Nat. Mater.*, 2018, **17**, 119–128.
58 H. Bristow, K. J. Thorley, A. J. P. White, A. Wadsworth, M. Babics, Z. Hamid, W. Zhang, A. F. Paterson, J. Kosco, J. Panidi, T. D. Anthopoulos and I. McCulloch, *Adv. Electron. Mater.*, 2019, **5**, 1900344.
59 C. Hammond, *The Basics of Crystallography and Diffraction*, International Union of Crystal, 2015.
60 B. R. Luginbuhl, P. Raval, T. Pawlak, Z. Du, T. Wang, G. Kupgan, N. Schopp, S. Chae, S. Yoon, A. Yi, H. Jung Kim, V. Coropceanu, J. L. Bredas, T. Q. Nguyen and G. N. M. Reddy, *Adv. Mater.*, 2022, **34**, e2105943.
61 M. Seifrid, G. Reddy, B. F. Chmelka and G. C. Bazan, *Nat. Rev. Mater.*, 2020, **5**, 910–930.
62 A. Karki, J. Vollbrecht, A. J. Gillett, S. S. Xiao, Y. L. Yang, Z. X. Peng, N. Schopp, A. L. Dixon, S. Yoon, M. Schrock, H. Ade, G. N. M. Reddy, R. H. Friend and T. Q. Nguyen, *Energy Environ. Sci.*, 2020, **13**, 3679–3692.
63 A. Karki, J. Vollbrecht, A. L. Dixon, N. Schopp, M. Schrock, G. M. Reddy and T. Q. Nguyen, *Adv. Mater.*, 2019, **31**, 1903868.
64 S. Sturniolo, T. F. Green, R. M. Hanson, M. Zilka, K. Refson, P. Hodgkinson, S. P. Brown and J. R. Yates, *Solid State Nucl. Magn. Reson.*, 2016, **78**, 64–70.
65 P. Hodgkinson, *Prog. Nucl. Magn. Reson. Spectrosc.*, 2020, **118**, 10–53.
66 J. Rivnay, S. C. Mannsfeld, C. E. Miller, A. Salleo and M. F. Toney, *Chem. Rev.*, 2012, **112**(10), 5488–5519.
67 Q. Liang, X. Jiao, Y. Yan, Z. Xie, G. Lu, J. Liu and Y. Han, *Adv. Funct. Mater.*, 2019, **29**, 1807591.
68 J. Hong, M. J. Sung, H. Cha, C. E. Park, J. R. Durrant, T. K. An, Y.-H. Kim and S.-K. Kwon, *ACS Appl. Mater. Interfaces*, 2018, **10**, 36037–36046.
69 J. Xu, F. Lin, L. Zhu, M. Zhang, T. Hao, G. Zhou, K. Gao, Y. Zou, G. Wei and Y. Yi, *Adv. Energy Mater.*, 2022, 2201338.
70 D. Bartesaghi, I. D. C. Pérez, J. Kniepert, S. Roland, M. Turbiez, D. Neher and L. Koster, *Nat. Commun.*, 2015, **6**, 1–10.
71 P. Kaienburg, U. Rau and T. Kirchartz, *Phys. Rev. Appl.*, 2016, **6**, 024001.

72 A. Baumann, J. Lorrmann, D. Rauh, C. Deibel and V. Dyakonov, *Adv. Mater.*, 2012, **24**, 4381–4386.
73 J. Gorenflot, M. C. Heiber, A. Baumann, J. Lorrmann, M. Gunz, A. Kämpgen, V. Dyakonov and C. Deibel, *J. Appl. Phys.*, 2014, **115**, 144502.
74 D. Murthy, A. Melianas, Z. Tang, G. Juška, K. Arlauskas, F. Zhang, L. D. Siebbeles, O. Inganäs and T. J. Savenije, *Adv. Funct. Mater.*, 2013, **23**, 4262–4268.
75 S. Chen, K. R. Choudhury, J. Subbiah, C. M. Amb, J. R. Reynolds and F. So, *Adv. Energy Mater.*, 2011, **1**, 963–969.
76 A. Baumann, T. J. Savenije, D. H. K. Murthy, M. Heeney, V. Dyakonov and C. Deibel, *Adv. Funct. Mater.*, 2011, **21**, 1687–1692.
77 G. Dennler, A. J. Mozer, G. Juška, A. Pivrikas, R. Österbacka, A. Fuchsbauer and N. S. Sariciftci, *Org. Electron.*, 2006, **7**, 229–234.
78 A. J. Mozer, N. S. Sariciftci, L. Lutsen, D. Vanderzande, R. Österbacka, M. Westerling and G. Juška, *Appl. Phys. Lett.*, 2005, **86**, 112104.
79 O. J. Sandberg and M. Nyman, *Org. Electron.*, 2019, **64**, 97–103.
80 G. Lakhwani, A. Rao and R. H. Friend, *Annu. Rev. Phys. Chem.*, 2014, **65**, 557–581.
81 T. P. Chaney, A. J. Levin, S. A. Schneider and M. F. Toney, *Mater. Horiz.*, 2022, **9**, 43–60.
82 B. A. Collins and E. Gann, *J. Polym. Sci.*, 2022, **60**, 1199–1243.
83 B. A. Collins, Z. Li, J. R. Tumbleston, E. Gann, C. R. McNeill and H. Ade, *Adv. Energy Mater.*, 2013, **3**, 1.
84 J. S. Park, G. U. Kim, D. Lee, S. Lee, B. Ma, S. Cho and B. J. Kim, *Adv. Funct. Mater.*, 2020, **30**, 2005787.
85 A. T. Yiu, P. M. Beaujuge, O. P. Lee, C. H. Woo, M. F. Toney and J. M. Frechet, *J. Am. Chem. Soc.*, 2012, **134**, 2180–2185.
86 W. Li, S. Albrecht, L. Yang, S. Roland, J. R. Tumbleston, T. McAfee, L. Yan, M. A. Kelly, H. Ade and D. Neher, *J. Am. Chem. Soc.*, 2014, **136**, 15566–15576.
87 S. Wilken, D. Scheunemann, S. Dahlström, M. Nyman, J. Parisi and R. Österbacka, *Adv. Electron. Mater.*, 2021, **7**, 2001056.
88 M. Azzouzi, T. Kirchartz and J. Nelson, *Trends Chem.*, 2019, **1**, 49–62.
89 K. D. Rosenthal, M. P. Hughes, B. R. Luginbuhl, N. A. Ran, A. Karki, S. J. Ko, H. Hu, M. Wang, H. Ade and T. Q. Nguyen, *Adv. Energy Mater.*, 2019, **9**, 1901077.
90 K. Vandewal, K. Tvingstedt, A. Gadisa, O. Inganäs and J. V. Manca, *Nat. Mater.*, 2009, **8**(11), 904–909.
91 J. Benduhn, K. Tvingstedt, F. Piersimoni, S. Ullbrich, Y. Fan, M. Tropiano, K. A. McGarry, O. Zeika, M. K. Riede, C. J. Douglas, S. Barlow, S. R. Marder, D. Neher, D. Spoltore and K. Vandewal, *Nat. Energy*, 2017, **2**, 17053.
92 L. Ye, H. Hu, M. Ghasemi, T. Wang, B. A. Collins, J.-H. Kim, K. Jiang, J. H. Carpenter, H. Li and Z. Li, *Nat. Mater.*, 2018, **17**, 253–260.
93 Y. Qin, Y. Xu, Z. Peng, J. Hou and H. Ade, *Adv. Funct. Mater.*, 2020, **30**, 2005011.
94 L. Ye, S. Li, X. Liu, S. Zhang, M. Ghasemi, Y. Xiong, J. Hou and H. Ade, *Joule*, 2019, **3**, 443–458.
95 W. Köntges, P. Perkhun, J. Kammerer, R. Alkarsifi, U. Würfel, O. Margeat, C. Videlot-Ackermann, J.-J. Simon, R. R. Schröder and J. Ackermann, *Energy Environ. Sci.*, 2020, **13**, 1259–1268.

